Basin Delineation with a 40-Hour Passive Seismic Record

by Elmer Ruigrok, Xander Campman, and Kees Wapenaar

Abstract   Several geophysical methods exist to delineate the lower interface of a sedimentary basin. Most popularly employed are gravity and magnetic surveys and surface-wave inversion. While all three methods are successful overall in estimating an average basin depth, they fail to find a more detailed depth variation. As an alternative, we consider three passive seismic techniques, using especially body waves. We analyze 40 hours of data, recorded with 110 stations installed over the Abu Gharadig basin in Egypt. In an earlier study we found the frequency band of 0.09–1.0 Hz to be dominated by body waves. As a first method we apply body-wave seismic interferometry (SI). Using body-wave noise, we extract *PP* and *SS* reflections from the basin floor. We estimate the depth of the basin to be around 4.8 km. As a second technique we estimate the resonance spectra of the basin, using the horizontal-to-vertical (H/V) spectral ratio. Using surface-wave noise, we find an extremum that is probably related to the complete sedimentary package. Using this peak, we find a basin depth of 5.4 km. Using *S*-phase arrivals, we find two extrema in the H/V, which are probably related to the *S*-wave resonances of two distinct layers in the basin. As a third method we compute receiver functions (RFs). Based on the RFs, we can confirm the presence of a large interface in the upper crust, but we cannot well constrain its depth.

Introduction

After centuries of exploration, the world distribution of sedimentary basins is largely known (St. John *et al.*, 1984). Especially the search for aquifers and hydrocarbon-bearing formations has contributed to this knowledge. Basins are currently not only used for extracting valuable resources, but also as storage places of undesired gases (Bachu, 2003). The overall architecture of a basin might be very complicated due to, for example, a rifting process that initiated its formation. For assessing the resource or storage potential of a basin, its dimensions play an important role. The spatial variation of total sediment thickness is also important for hazard assessment. It can be used for computing the possible amplification of earthquake-induced ground motion (Herak, 2008). The thickness of the sediment package is also important for studies of the lower crust and mantle. A correction needs to be made for the basin before information of underlying rock can be unveiled. The vertical dimensions of a basin, however, are hard to constrain and might show large lateral discontinuities that are not easily resolved.

The lower interface, which is most commonly a contrast between sedimentary deposits and underlying crystalline rock, is a significant marker that shows up as a large signal in different geophysical measurements. Generally, crystalline rocks have a much higher density than sedimentary rocks. Therefore, the depth of the basin can be estimated from gravity measurements (Barbosa *et al.*, 1997). Also, the basement rock contains a much larger amount of magnetic rock than

the overlying sediments. Hence, the depth of the basement can be estimated from magnetic measurements (Salem *et al.*, 2008). Both with gravity and magnetic methods the depth is quite poorly constrained as assumptions need to be made about the density or magnetic susceptibility of the basement. The basin–basement interface is also a large elastic impedance contrast, which makes it amenable to seismic detection. An advantage of seismics is that only material properties of the sediment need to be known to find an accurate depth estimate of the basin–basement interface. However, the waves that are induced in a conventional surface-seismic campaign have a frequency band too high to reach the lower portions of deep onshore basins. Even if they make it all the way down and up again, the waves have undergone multiple scattering that is difficult to use for reflection imaging. Using low-frequency sources is possible, but very costly. Therefore, we look into passive seismic techniques.

In this study we process data collected with a densely sampled seismic array in the northeast Abu Gharadig basin. This basin is located in the Western Desert in Egypt. It is part of a string of hydrocarbon-bearing basins that cover the northeastern margin of Africa and share a similar history (Bosworth *et al.*, 2008). These basins were formed in the Jura, during the break up of supercontinent Pangaea. The Abu Gharadig is one of the more complex basins due to inversion of part of the extensional faults. This inversion occurred when the tectonic regime became compressional,

when Africa started moving toward Eurasia. As a consequence, the basement depth varies significantly over the different basin blocks.

We restrict our data to a 40-hour period in which all stations were synchronically recording. In an earlier analysis of the same data (Ruigrok *et al.*, 2011) we split up the low-frequency data into three distinct frequencies, the single frequency (SF) band 0.03–0.09 Hz, the double frequency (DF) band 0.09–0.5 Hz, and the Mediterranean frequency (MF) band 0.4–1.0 Hz. The analysis showed the SF band is dominated by surface-wave noise coming from the south-southwest, while the DF and MF bands are dominated by body-wave noise coming from the southwest and northwest, respectively. The higher frequencies ($f > 1.0$ Hz) are dominated by surface-wave noise from the northeast.

In principle, surface-wave noise can be used to obtain estimates of the basin depth. Toksöz (1964) and Asten and Henstridge (1984) estimated phase velocities directly from surface-wave noise. From the estimated dispersion curve they inverted for the basin depth. The errors turned out to be significant. Nowadays, the phase velocities can be more accurately determined by first applying seismic interferometry to the surface-wave noise (Shapiro *et al.*, 2005). Still, the inversion of the phase velocities gives a limited resolution in depth, which makes it less suitable for our delineation purposes. Besides, we lack a sufficient recording of surface waves in the required frequency band. From the literature (Bosworth *et al.*, 2008) it is known that the basin–basement interface must be at a depth of about 5 km. This interface is too deep to be resolved from the dispersion of surface waves with frequencies above 1 Hz and too shallow for frequencies below 0.09 Hz (e.g., Xia *et al.*, 1999).

The dominance of body waves in the low-frequency noise makes the Egypt dataset excellent for comparing a few body-wave seismic techniques for basin delineation. In this study we consider three techniques: body-wave seismic interferometry (SI), body-wave horizontal-to-vertical (H/V) ratio, and radial-component receiver function (RF). The working principle of these three methods is shown in Figure 1. Seismic interferometry (Schuster, 2009; Wapenaar *et al.*, 2010) can be seen as a filtering operation. Seismic records at two stations are cross correlated. When the records contain waves that traveled between both stations, these waves are passed, while all other waves are suppressed. For example, when a record contains reflected travel paths between a station at $\mathbf{x}_{\mathcal{A}}$ and $\mathbf{x}_{\mathcal{B}}$ (Fig. 1a, left) only the stationary reflection path between the two stations is passed, with the path between the actual source and one of the stations removed, while all the other arrivals are suppressed, given an adequate distribution of (noise) sources. After applying SI effectively, a response is obtained as if a source existed at one of the stations (Fig. 1a, right). By extracting many of these reflection responses at different offsets, a velocity model can be derived, and the depth of the reflectors can be found.

Body-wave H/V ratio (Nakamura, 2000) is a division of the amplitude spectra of body-wave noise recorded on the
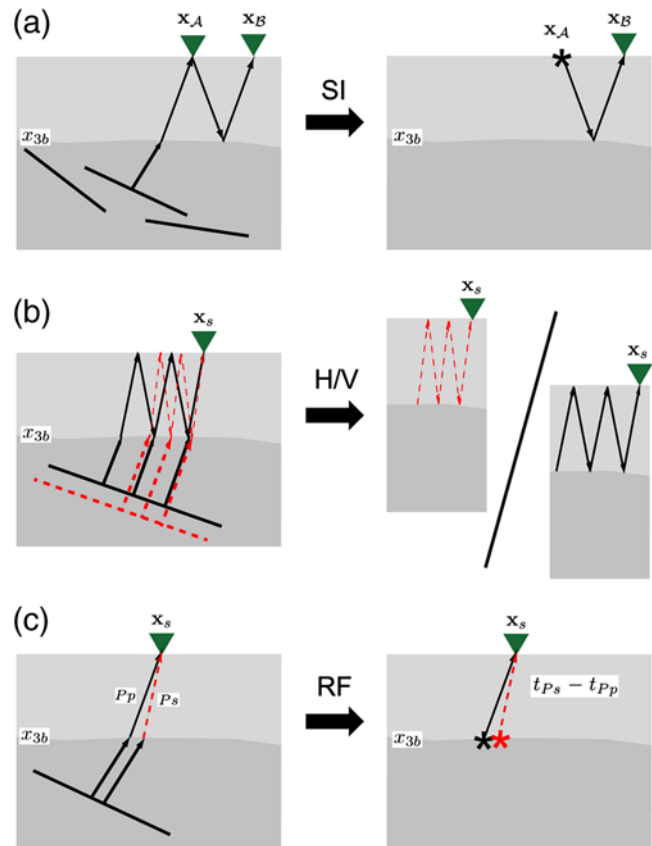

Figure 1.   A cartoon illustration of the three passive seismic techniques that are considered in this study: (a) body-wave seismic interferometry (SI), (b) body-wave horizontal-to-vertical (H/V) ratio, and (c) receiver function (RF). For each technique, the input (left) and output (right) are shown for a one-layer-over-a-half-space model (basin overlying a basement), with receivers (triangles) on the Earth's surface. The illumination is from below with plane *P*- (solid line) and or *S*-waves (dashed line). From the plane-wave illumination, lines with arrows indicate the rays relevant to the receivers. Stars on the right upper and lower panels denote effective line sources. Subscripts $\mathcal{A}$ and $\mathcal{B}$ denote two different stations. Subscript *s* indicates that the station is on the free surface. The depth level of the basin–basement interface is shown by x_{3b}. The color version of this figure is available only in the electronic edition.

horizontal and vertical component. Through the division, source effects are largely removed. If *P*- and *S*-wave noise is used with a near-planar incidence (Fig. 1b, left), then H/V approximates the ratio of the *S*-wave and *P*-wave amplification spectra (Fig. 1b, right). This latter ratio can be inverted to derive layer properties of the top layer(s) (Herak, 2008).

Receiver function (Langston, 1979) is also a ratio between a horizontal and vertical seismogram. However, RF is a complex spectral division. Through this deconvolution, source effects are removed from the horizontal component. If a time window is selected around the *P*-phase arrival of a distant earthquake, the vertical component will primarily detect *P* waves (most prominently *Pp*), while the horizontal component will primarily register *P-S* converted waves (most prominently *Ps*, see Fig. 1c, left). The deconvolution result is

called the receiver function. From this resulting trace, the travel-time difference of *P* and *S* waves ($t_{P_s} - t_{P_p}$) can be read (Fig. 1c, right). When velocity information is available, this travel-time difference can be used to find the depth of the layer(s).

Seismic interferometry is only very recently being developed and is considered for extracting Earth structure at many different scales (e.g., Galetti and Curtis, 2011). Seismic interferometry may be applied to only one station, but more regularly, data at different stations are combined. The H/V is most popularly employed for constraining near-surface *S*-wave models for geotechnical purposes, but it has also been applied for basin studies (Martini *et al.*, 2011). Receiver function is especially used for delineating structure in the lower crust and upper mantle. Both H/V and RF were developed as single station operations.

In this study we will first briefly analyze the 40-hour noise record. This noise analysis is required to determine what parts of data are to be used as input for the different passive seismic techniques. In the remainder, we will apply the different techniques (SI, H/V, and RF) to the data with the aim to delineate the basin–basement interface. Through this exercise we are learning which techniques are best fit for this purpose.

Noise Analysis

The location of the seismic array, which will be denoted with the Egypt array in the following, is about 230 km west of Cairo. While the area is unpopulated, there is some activity related to oil and gas production. During the day, several dirt tracks in the area are being used by traffic from local producers. The nighttime is very quiet.

Figure 2 shows the geographical setting and the receiver layout. A total of 110 broadband three-component seismometers (Trillium T40) were placed in five parallel lines and three cross lines at varying angles. Inline interstation spacing was 500 m, with a more densely sampled (350 m) area in the middle of the array. In total, about 60 hours of noise were simultaneously recorded on all 110 stations.

We restrict our data to a 40-hour period starting 12 October 2009. Figure 3 depicts the power spectrum density (PSD) variation for these 40 hours and for all three components. The energy that is fairly constant over time is related to microseisms, while the transient events are caused by earthquakes. For more details, see Ruigrok *et al.* (2011). In this same reference we classified the noise in three distinct frequency bands, encompassing different types of microseism (the SF, DF, and MF bands, see Fig. 3). We found that the *Z*-component (vertical component) noise in the higher frequency band (the MF band 0.4–1.0 Hz) could be used to retrieve reflections from the upper crust. In this section we restrict ourselves to this higher frequency band. We will study the waveform content of all three components.

First, we split up the 40-hour records in 5-minute windows. For each time window we estimate the dominant ray
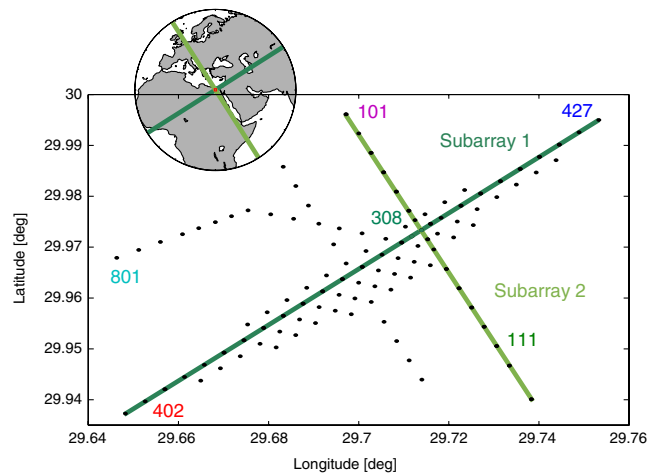

Figure 2. The layout of the Egypt array and the geographic setting (inset). The station positions are indicated with dots. For a few specific stations, the station numbers are given. Two linear subarrays are denoted with straight lines that are plotted in the inset. The color version of this figure is available only in the electronic edition.

parameter p_{dom} and back azimuth θ_{dom} (dominant illumination) through beamforming (Lacoss *et al.*, 1969). A single time window might simultaneously pick up noise from different directions and distances. Therefore, we also estimate the second most dominant back-azimuth and ray-parameter combinations (subdominant illumination). Figure 4 shows these estimated dominant and subdominant waveform distributions in ray parameter–back azimuth space. We leave out the *E* component, because the distributions are fairly similar for the horizontal components.

The array response is not perfect over the complete (p, θ) space under consideration. Consequently, a single plane wave maps to a main lobe at the true (p, θ) coordinate, but also to small side lobes (aliasing). For the *Z* component, the subdominant illumination maps primarily to the aliased side lobes of the dominant illumination (see the symmetry). Hence, the time windows may be assumed to be dominated by one plane wave only. The horizontal components, on the other hand, show a rich distribution of subdominant illumination that is not due to aliased side-lobes of the dominant illumination. Hence, for the horizontal components, subdominant illumination cannot be neglected.

Figure 4 maps the ray parameters of a number of crustal phases to ease identification of the detected waveforms. When considering distant sources near the Earth's surface, all time windows that map to points within the *Pn*- and *Sn*-ring must be dominated by teleseismic or global *P*-wave and *S*-wave phases. For a description of the phases, see, for example, Storchak *et al.* (2003). Fundamental-mode Rayleigh wave (*LR*) and fundamental-mode Love wave (*LQ*) have relatively low velocities and hence high ray parameters. This is due to the basin setting of the array and the relatively high frequencies of the MF band noise.
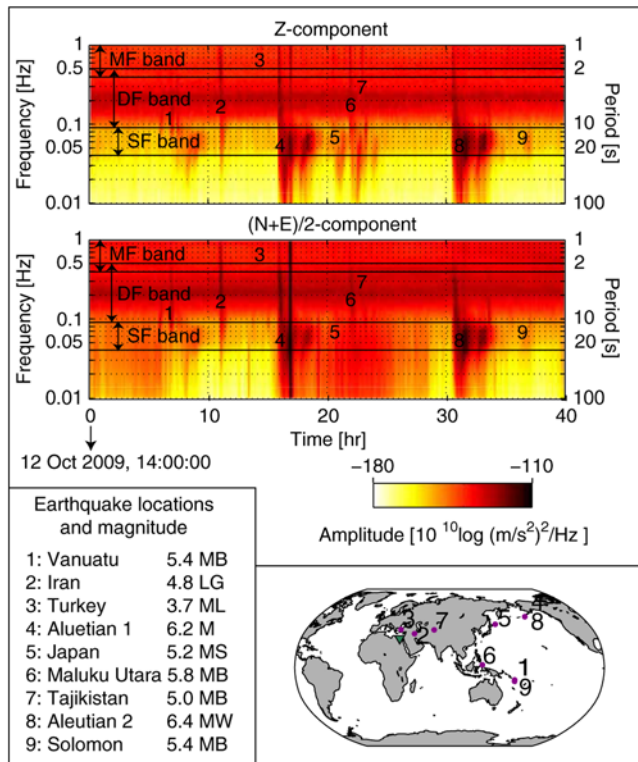
Figure 3. The noise spectrograms (upper box) for the vertical (Z) and an average of the horizontal [$(N + E)/2$] components, made up by a concatenation of power-spectrum densities based on 10-minute records detected at station 402. The transient events are caused by earthquakes. The identified earthquakes and their magnitudes (given in various scales) are listed in the lower-left box and are indicated on the spectrograms. Their locations are plotted on a world map (lower right box). The data between 0.03 and 1.0 Hz are divided into three frequency bands (MF, DF, and SF) marking different characteristics of the noise in the various bands. The color version of this figure is available only in the electronic edition.

Judging from Figure 4a, the noise on the Z component contains primarily global and teleseismic phases, but also some regional phases. The back-azimuth range is quite narrow and points toward microseismic sources in the Mediterranean and North Atlantic, and possibly even the North Pacific.

The ray parameters on the horizontal components are significantly larger (Fig. 4b) and can be explained by a mix of lithospheric phases, *Sg*, *Lg*, and *Sn* (Isacks and Stephens, 1975). It turns out that the horizontal components do not pick up body waves induced by primary sources in the North Atlantic and North Pacific. The back-azimuth range for the horizontal components is much larger than the range of the *P* waves. Moreover, this back-azimuth range shows a clear correlation with the coasts near the Egypt array (compare Fig. 4b with the inset in Fig. 2). Thus, it seems that the horizontal components pick up mostly lithospheric phases from nearby coasts (Mediterranean coast in the northwest and the Red Sea coast in the east-southeast), which are either directly induced near the coast or converted at the ocean-continent transition.

Body-Wave Seismic Interferometry

In this section we show results of applying SI to noise detected at subarray 2 (Fig. 2). Three-component particle-velocity noise recordings in principle allow the reconstruction of nine components of the Green's functions between two station locations, $\mathbf{x}_A$ and $1\mathbf{x}_B$, where $\mathbf{x} = (x_1, x_2, x_3)$ denotes a position vector, and the subscripts A and B distinguish two different stations when their position vectors are not written out explicitly. Each component of the Green's function is the combination of a traction source at $\mathbf{x}_A$ in one of the orthogonal directions and a particle-velocity sensor at $\mathbf{x}_B$ in one of the orthogonal directions (Wapenaar and Fokkema, 2006). In our case, the vertical component detects different wave fields than the horizontal components (Fig. 4). Consequently, cross correlations between these components are extremely noisy, contain little to no subsurface information, and are thus omitted. Also we leave out combinations between the radial and transverse component. Hence, we only retrieve the vertical, radial, and transverse particle-velocity responses due to vertical, radial, and transverse traction sources, respectively. Details about interferometrically processing the Z-component noise can be found in Ruigrok et al. (2011). Applying SI to the horizontal components involves an additional preprocessing step, which is the rotation of the noise records from north (N) and east (E) to radial (R) and transverse (T). To ease processing, we define R and T with respect to subarray 2, rather than the (varying) source. For the horizontal components, only time windows are used with dominant sources approximately inline with subarray 2. Time windows with θ_{dom} varying up to 20° from the subarray orientation are still accepted. Therefore, effectively, R and T are still closely related to the back azimuth of the actual (primary) source. For the Z-component noise panels, a back-azimuth filter is not required because the illumination is already restricted to back azimuths close to the orientation of subarray 2 (Figs. 2, 4a).

Figure 5 shows the retrieved responses for a virtual source at the location of station 609 and receivers at all station positions of subarray 2. To interpret the different events we started off with the regional model from the Cornell Middle East and Africa Project (Seber et al., 1997) and adjusted it to correspond to the data. This model contains *P*-wave velocity information down to the upper mantle. However, the different basin blocks, as have been interpreted in, for example, Bosworth et al. (2008), have been averaged out. Consequently, the largest change is increasing an average basin depth from the regional model (3 km) to a local basin depth of 4.8 km. This is not an unreasonable adjustment, considering that nearby oil-bearing sediments were found at depths below 3 km (Franssen and Hoogerduijn-Strating, 2006; Hoogerduijn-Strating and Postuma, 2008). For this updated model (Fig. 5a) we compute travel-time curves for the most prominent reflections and overlay these to the retrieved responses (Fig. 5b–e). *PP* is the two-way travel-time curve of a primary *P*-wave reflection from the basin floor, whereas
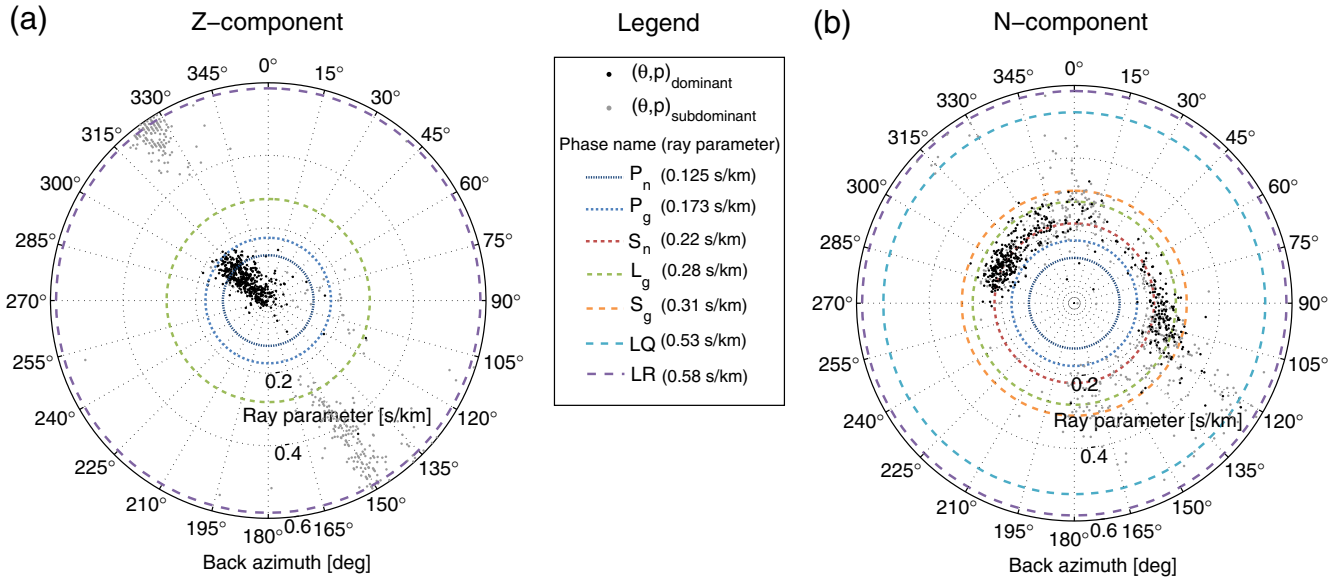
Figure 4. The estimated dominant (black dots) and subdominant (gray dots) illumination for the (a) *Z*- and (b) *N*-component noise, respectively. One dot in the ray parameter–back azimuth space corresponds to the plane-wave direction and angle of incidence with the largest (or second largest) beampower. The beampower is obtained by beamforming 5-minute time windows, frequency limited between 0.4 and 1.0 Hz. For interpretation, ray parameters of common regional phases (see legend) have been added to the radar displays. The color version of this figure is available only in the electronic edition.

SS and *PPPP* denote the travel-time curve for the same interface, of an *S*-wave reflection and *P*-wave multiple, respectively. *PS* and *SP* are the *P-S* and *S-P* converted reflections on the basin–basement interface, respectively. The solid lines in Figure 5b–e denote the travel times after which physical retrievals may be expected, given the used illumination range (see Ruigrok *et al.*, 2010). This is called the response-restriction function in the following. For the *Z*-component noise we used only time windows with $|p_{\mathrm{dom}}| < 0.08$ s/km, while for the horizontal-component noise we used time windows with dominant absolute ray parameters up till 0.35 s/km. Because a larger illumination range was used
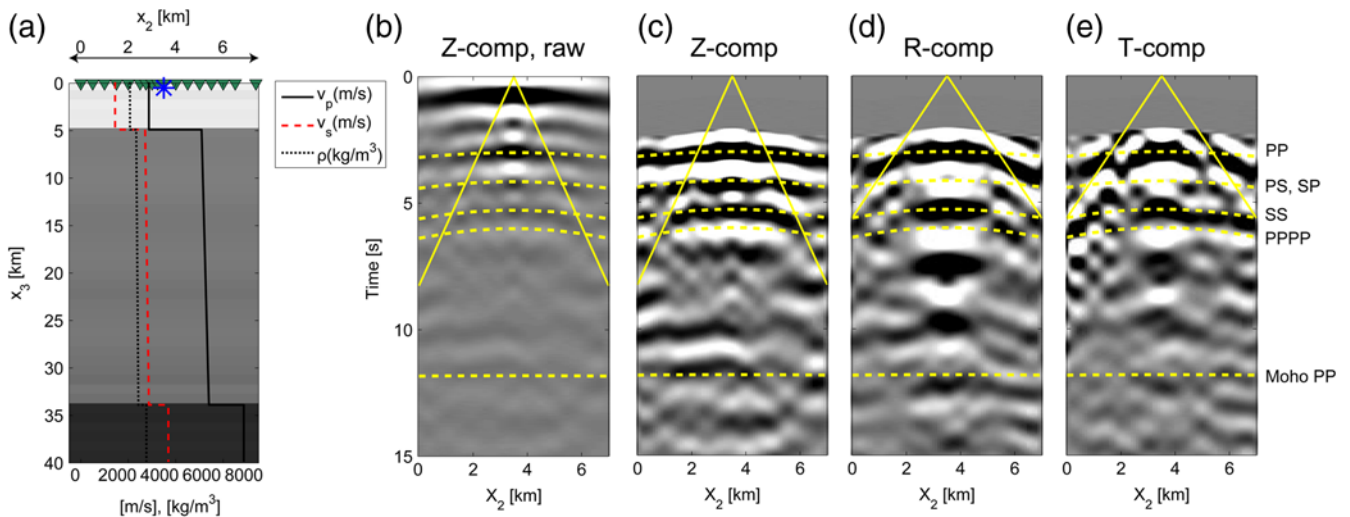

Figure 5. (a) In gray shading, a *P*-wave velocity model of the crust below the Egypt array, augmented with a depth profile of the *P*-wave (solid line) and the *S*-wave (dashed line) velocity and the density (dotted line). The triangles on the top of the figure denote the station locations of subarray 2. The virtual source station is overlain by a star. (b) The result after applying seismic interferometry to *Z*-component noise, for a virtual source at station 609 and receivers at all stations of subarray 2. (c) The same retrieved response as (b) after muting the (spurious) direct wave. (d) and (e) The retrieved responses using *R*- and *T*-component noise, respectively. On (c)–(e) the thick black lines border a fan within which physical retrievals may be expected. The dashed lines are two-way travel-time curves for a few prominent reflections, which were computed using (a). The color version of this figure is available only in the electronic edition.

for the horizontal components, at a larger part of the $t - x$ space, physical retrievals may be expected.

The effective wavelet is a flipped Ricker wavelet (white-black-white) possibly with some additional ringing (Ruigrok et al., 2010). If the ringing was severe, this would lead to ghost arrivals in the retrieved responses (Fig. 5c–e). These ghost arrivals would show up as repetitions of a main arrival. The repetitions would have the same moveout $[dt(x)/dx]$ as the main arrival. The general trend, though, in Figure 5c–e is smaller moveouts for events at larger times. This is the travel-time behavior that is expected for (primary) reflections.

For all components, PP is clearly retrieved. On the vertical component (Fig. 5c), this reflection has a realistic moveout over much of the considered offset range. For the horizontal retrievals (Fig. 5d,e), at larger offsets, the moveout behavior of the retrieved reflection deviates from the expected travel-time function. This might be due to interference with guided waves. PS and SP seem to be weak and cannot be clearly distinguished. The next clear event in Figure 5c–e (at about 5.5 s) could be explained by either a P-wave multiple from the basin–basement interface or an S-wave primary from the same reflector. On the horizontal components the event arrives just too late to be PPPP, but it fits well with SS when a 1.8 v_P/v_S ratio is taken, which is a common value for consolidated sediments. On the vertical component it is ambiguous whether PPPP, SS, or a combination of the two, is retrieved. Figure 6a shows a comparison of the retrieved responses for coinciding source and receiver positions for the three components. The P-wave reflection has a higher relative amplitude on the Z component, while the S-wave reflection has a higher relative amplitude on the horizontal components.

Figure 5b–e shows the responses for a single source and multiple receiver positions. Each receiver is at a different offset from the source, and therefore the reflections points in the subsurface differ. Only when the subsurface does not vary laterally, this representation of the data can be used for velocity analysis. To improve the velocity analysis we resort to the Z-component retrievals in a response for which the reflection points are approximately the same for the different traces. Figure 6b shows one resulting common-midpoint gather (Yilmaz and Doherty, 2000). It can be seen that with this representation the modeled PP and SS/PPPP better fit with the data. Note that the timing and moveout of the retrieved PP and SS/PPPP largely correspond with the forward modeled curves (dashed lines) within the range where physical retrieval are expected (range is bounded by the solid lines). The velocities cannot be estimated with high precision, however, due to the limited offset range, the limited bandwidth, and the small illumination artifacts.

Bosworth et al. (2008) analyzed gravity data and seismic sections for basins in northeast Africa. They interpreted the Abu Gharadig basin to be around 5-km deep near the array. From the retrieved reflections we find a basin depth of 4.8 km (Fig. 5a). The Moho reflection is expected to arrive around a two-way travel time of 12 s, with an almost flat
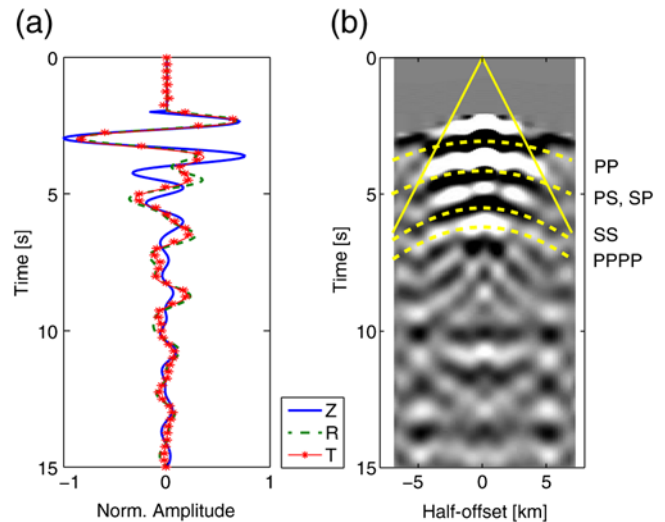

Figure 6. (a) The middle traces from Figure 5c–e, and (b) the Z-component common-midpoint gather for a midpoint coinciding with the middle station in subarray 2. The color version of this figure is available only in the electronic edition.

moveout. In Figure 5c–e some near-flat events can be seen around this time. However, the amplitudes are too low for interpretation.

As a final processing step, we retrieve the $Z - Z$ reflection responses for coinciding source and receiver positions at every station of the array, using the same data selection as was used for obtaining Figure 5c. Subsequently, we determine the timing of the retrieved P-wave basement reflections $[t(\mathbf{x}, h0)_{PP}^{basin}]$. Figure 7 shows a cubic interpolation of the picked arrival times. All stations used in the interpolation are shown as black dots. It turns out that the spatial time differences are minimal for the P-wave reflection. The dynamic
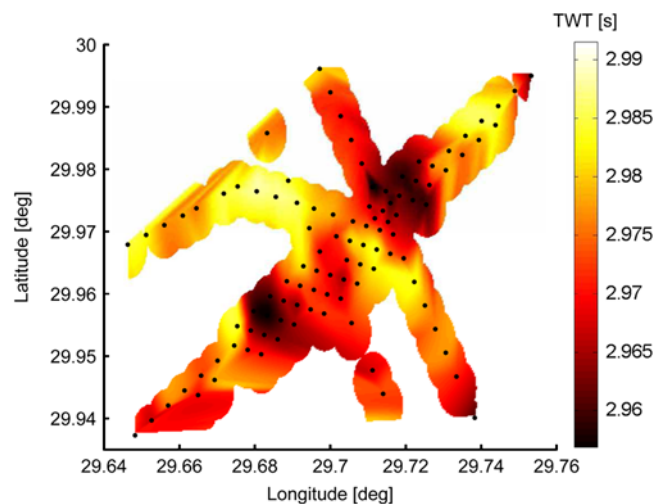

Figure 7. Top-basement interpolated two-way P-wave travel times (TWT) for coinciding source and receiver positions. The color version of this figure is available only in the electronic edition.

range is 0.03 s, which would map to basement-top undulations of maximally 96 m using the average estimated P-wave velocity of 3.2 km/s. However, the timing differences may be as well described to lateral variations in sediment infill rather than basin-depth variations. The discontinuous nature of the lateral variations could be caused by faulting within the basin.

H/V Ratio

It is well known that a spectrum of a reflection response contains many notches, even if the source had a flat spectrum. These notches are due to the resonances of the different layers. The resonance or amplification spectrum for S and P waves can be computed for an arbitrary stack of layers overlying a homogeneous half-space (Herak, 2008). Vice versa, medium properties of the layers can be inverted from a measured amplification spectrum.

Noise Records

We assume a simple model of a one-layer sedimentary basin overlying a homogeneous half-space, the basement. The observed P-wave and S-wave amplitude spectra can be written as

$$|\hat{v}^P(\mathbf{x}_s, f)| = |\hat{G}^P(\mathbf{x}_s, x_{3b}, f)\hat{G}^P(x_{3b}, \mathbf{p}_{\text{dom}}^P, f)\hat{N}_{\text{dom}}^P(f)|, \quad (1)$$

$$|\hat{v}^S(\mathbf{x}_s, f)| = |\hat{G}^S(\mathbf{x}_s, x_{3b}, f)\hat{G}^S(x_{3b}, \mathbf{p}_{\text{dom}}^S, f)\hat{N}_{\text{dom}}^S(f)|, \quad (2)$$

where f is the frequency, x_{3b} denotes the depth level of the basement below the array, and $\mathbf{x}_s$ denotes a surface-position vector. The hat above the quantities denotes that they are in the frequency domain. The right side of equations (1) and (2) contain three terms. The far-right term, $\hat{N}_{\text{dom}}$, is the spectrum of the dominant noise source. The middle term is the Green's function describing the propagation of the dominant phase, parameterized with $\mathbf{p}_{\text{dom}} = (p_{\text{dom}}, \theta_{\text{dom}})$, to the basement below the array. Finally, the left term describes the propagation through the sedimentary basin. The transmission coefficients between the basement and basin have been left out, because they do not significantly affect the shape of the measured spectra. For the same reason, P-S and S-P conversions have been left out.

$|\hat{G}^{P,S}(\mathbf{x}_s, x_{3b}, f)|$ is the P-wave, S-wave (amplification) spectrum of the sedimentary basin. In the following, we try to find this spectrum from the measurements. First, we approximate the P-wave and S-wave spectra with the vertical- and transverse-component spectra, respectively. For this approximation to hold, we would need to select data with almost vertical incidence. Second, we assume that no serious resonances occur, at least not in the frequency band of interest, before the waves enter the sedimentary basin. With this assumption, $\hat{G}^{P,S}(x_{3b}, \mathbf{p}_{\text{dom}}^{P,S}, f)$ has a flat spectrum in equations (1) and (2), and can be left out, yielding:

$$|\hat{v}^Z(\mathbf{x}_s, f)| \approx |\hat{G}^P(\mathbf{x}_s, x_{3b}, f)\hat{N}_{\text{dom}}^P(f)|, \quad (3)$$

$$|\hat{v}^T(\mathbf{x}_s, f)| \approx |\hat{G}^S(\mathbf{x}_s, x_{3b}, f)\hat{N}_{\text{dom}}^S(f)|. \quad (4)$$

Still, in equations (3) and (4) the resonance spectra of the basin are obscured by the noise spectra. To remove this latter influence, we would need to select time windows where the P- and S-wave noise spectra are similar. This would be achieved when all components are picking up noise from the same source areas. Using these time windows, we divide the measured transverse-component (amplitude) spectrum by the vertical-component spectrum to obtain the H/V(f) ratio, a common technique (Nakamura, 2000):

$$\text{H/V}(f) = \frac{|\hat{v}^T(\mathbf{x}_s, f)|}{|\hat{v}^Z(\mathbf{x}_s, f)|} \approx \frac{|\hat{G}^S(\mathbf{x}_s, x_{3b}, f)|}{|\hat{G}^P(\mathbf{x}_s, x_{3b}, f)|}. \quad (5)$$

At the low-frequency side, this ratio is colored by the first resonance frequency f_0 from the P- and S-wave amplification spectra. This resonance frequency can be expressed as (Tsai, 1970)

$$f_0^{P,S} = \frac{v_{P,S}}{4d}, \quad (6)$$

where d denotes the thickness of the layer, and $v_{P,S}$ denotes the P-wave or S-wave velocity. Hence, from $f_0^{P,S}$ the depth of the basin can be computed when average velocities are known for the basin.

We select a 5-hour interval of noise (hours 35–40, see Fig. 3), where θ_{dom} is similar for all components. We rotate the data using θ_{dom} (305°) to obtain a radial and transverse component. We also consider the frequency band 0.06–0.9 Hz. Though there is contamination, it can be assumed that P and S waves dominate noise on the Z and T components, respectively (see figures 7 and 13 from Ruigrok *et al.*, 2011), at least for frequencies higher than 0.09 Hz. P-wave leakage to the T component and S-wave leakage to the Z component lead to a size reduction of the peaks and troughs in H/V(f). Still, the overall shape remains. For the 5-hour time interval we compute the PSD for the Z and T component for six different stations at the different corners of the array (station 427, 11, 402, 801, 101, and 308; see Fig. 2). For the PSD computation we use 75% overlying segments with 2^{14} samples per segment. Subsequently, as a stable implementation of equation (5), we divide the T-component PSD by the Z-component PSD to obtain the horizontal-to-vertical spectral ratio. As a last step, we average the H/V(f) over the six stations.

Figure 8 shows both the H/V for the six individual stations (thin dashed lines) and the average H/V (thick line). f_0^P would lead to a notch in the H/V(f) ratio. However, it is hard to identify these minima in H/V(f), if present. f_0^P is always larger than f_0^S; therefore, H/V(f_0^P) is generally obscured by higher resonance frequencies in $|\hat{G}^S(\mathbf{x}_s, x_{3b}, f)|$. f_0^S would lead to a maximum in the H/V(f) ratio. These can be identified easily in Figure 8. Three clear resonance extrema can be seen at 0.085, 0.32, and 0.83 Hz. These peaks must be related to $|\hat{G}^S(\mathbf{x}_s, x_{3b}, f)|$. The first peak is likely at a fundamental resonating frequency. Using equation (6) with
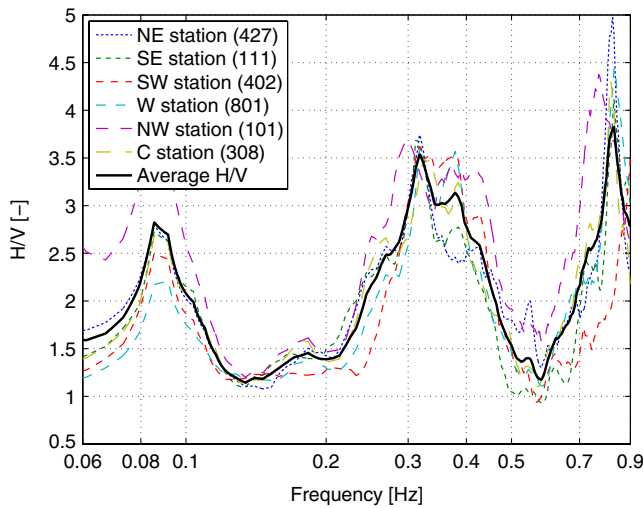
Figure 8. H/V ratio averaged over 5 hours of noise for 6 stations (thin dashed lines), at different corners of the array. With the same numbers these stations are indicated on Figure 2. The thick line denotes the H/V ratio averaged over the 6 stations. The color version of this figure is available only in the electronic edition.

$v_S = 1.85$ km/s (from model 5a) we find it is related to a resonating layer with a thickness of 5.4 km. This layer is most likely the complete sedimentary column. The two other extrema might be caused (partly) by higher resonating frequencies from the same layer or by other distinct resonating layers within the sedimentary column. If they were fundamental resonating frequencies from other layers, the layer thicknesses would be about 1.4 and 0.56 km. A probable model could be obtained through inversion (Herak, 2008). Because of wavemode complications (next paragraph), we leave out such inversion.

With H/V we estimate the basin depth to be 5.4 km. This is somewhat deeper than estimated with SI (4.8 km). The resonance peak is at a frequency (0.085 Hz), within the 0.03–0.09 Hz band, found to be dominated by surface waves (Ruigrok *et al.*, 2011). Therefore, it is surprising that the H/V ratio still gives a reasonable estimate of the basin depth. However, Lermo and Chávez-García (1994) show that the surface-wave H/V (ellipticity) has an extremum at f_0^s.

Earthquake Records

We also measured S-phase arrivals from earthquakes, in the frequency range where f_0^s related to the basin is expected. So, we can independently estimate f_0^s, as was empirically shown in Field and Jacob (1995). Their model is quite similar to the one for noise, expressed in equations (1)–(5). The main difference is that the noise source-spectra in equations (1) and (2) are replaced by earthquake source-spectra. Further, Field and Jacob (1995) assume that the vertical component, during the S-phase arrival, is dominated by S-P conversions. In this case, the term $\hat{G}^P(x_{3b}, \mathbf{p}, f)$ in equation (1) would need to be replaced by $\hat{G}^S(x_{3b}, \mathbf{p}, f)$. Using this change and previous approximations, we obtain equation (5) again.

We choose an earthquake that contains broadband S-phase arrivals (Aleutian 2, number 8 in Fig. 3), which occurred at 96.1° from the array. We select a 1000 s time window, which includes SKS, SKKS, and SS, and compute the PSD for the Z component and T component using the same recipe as before. The resulting PSDs are used to compute H/V(f). Figure 9 shows the resulting H/V(f) for the same six stations as in Figure 8. This time, two clear resonance extrema can be seen, one at 0.13 and one at 0.31 Hz. Again, these peaks must be related to $|\hat{G}^S(\mathbf{x}_s, x_{3b}, f)|$. Using equation (6) again with $v_S = 1.85$, we find two resonating layers with thicknesses of 3.6 and 1.5 km, respectively.

Comparison

When comparing Figures 8 and 9 we find large similarities in the middle frequency band, where both are dominated by body waves. With both methods the extremum at about 0.31 Hz is resolved. Note that the H/V(f) amplitudes are different. This is also expected, because the one method (Fig. 8) has direct P-wave illumination, while the other method (Fig. 9) has primarily S-P conversions on the vertical component. At the higher end of the frequency band, the noise H/V(f) (Fig. 8) has a clear peak, while the earthquake H/V(f) (Fig. 9) extremum is poorly developed. This is not unexpected, considering that for the earthquake H/V, especially, core phases were used, for which the higher frequencies are attenuated. At the lower end of the frequency band, both methods resolve a different extremum. The extremum found with the noise is indicative of the ellipticity of the surface waves. The ellipticity, for this frequency band, is governed by the complete sedimentary package, thus a thickness estimate of the complete package is resolved (5.4 km). The
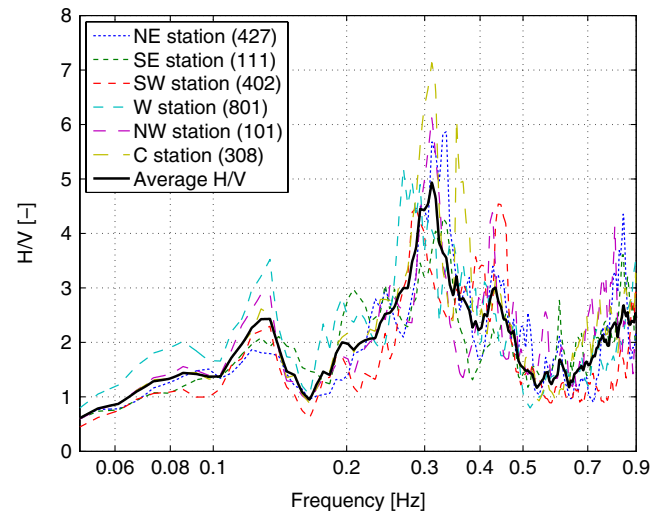

Figure 9. H/V ratio averaged over a 1000 s interval dominated by S-phases from the Aleutian 2 earthquake (Fig. 3, no. 8), for 6 stations (thin dashed lines), at different corners of the array. With the same numbers these stations are indicated on Figure 2. The thick line denotes the H/V ratio averaged over the 6 stations. The color version of this figure is available only in the electronic edition.

extremum found with the earthquake *S*-phase arrivals seem to be indicative of the resonance of a single layer within the sedimentary package. Based on this interpretation the basin thus seems to consist of two distinct layers with a thickness of 3.6 and 1.5 km, resulting in a total thickness estimate of 5.1 km.

Receiver Function

With the receiver function (RF) method a clean *P* or *S* phase from a distant earthquake is used (Langston, 1979). We will only apply it to *P*-phase arrivals, as the recorded *S*-wave phases are severely contaminated with *P*-wave coda. For a *P*-phase response it is assumed that all recorded *S* waves are due to conversions in the lithosphere below the stations. The RF can be seen as a scaled version of the *R* component, deconvolved for the source–time function and with the removal of *P*-wave multiples (Ammon, 1991). Consequently, on the RF, the arrival times of the converted waves with respect to the direct *P* wave can be picked. When a velocity model is known, the travel-time differences between the *P* wave and the subsequent *P-S* conversions can be used to find the depths of the interfaces.

The best receiver functions (RFs) are achieved when the *P* phase is recorded over a broad frequency band. This is the case for both the Aleutian 1 and 2 earthquakes (numbers 4 and 8 in Fig. 3). Figure 10 shows the RFs. On the left side the RFs are plotted for stations in subarray 2 (see Fig. 2). The RFs vary from station to station. For example, between 5 and 10 s two phases with a large moveout can be noticed. Because the subsurface may be assumed to be approximately layered for the offset range and frequencies considered, these phases are unlikely part of the RF. More likely, these phases are caused by microseism contamination. For both earthquakes there is still considerable microseism energy on the *Z* and *R* component. Consequently the RFs also will be affected. These microseism related events turned out to have the largest moveout on subarray 2. Therefore, the RFs are averaged over this subarray to yield the final RFs, as displayed on the right side in Figure 10.

We will attempt to explain the final RFs with the model obtained by adjusting a starting model with the SI results (Fig. 5a). The model contains a basin (depth = 4.8 km) and crystalline crust (depth = 34 km) overlying a homogeneous half-space (the mantle). To clearly identify the different phases, first we forward model a direct plane-wave *P*-wave response with a Ricker wavelet with a central frequency of 1.0 Hz (Fig. 11a). We use the ray parameter of the *P*-phase from the Aleutian responses (0.04 s/km). The synthetic response for this two-layer-over-a-half-space model contains just the direct *P* wave (*Ppp*), the conversion on the basement–basin interface (*Pps*), the conversion on the Moho (*Pss*), and the conversion on both interfaces (*Psp*). This last arrival has a negligible amplitude with respect to the other arrivals and is therefore hardly noticeable in Figure 11. The *R* component in Figure 11a is hard to interpret due to the complicated source–time function used in the forward mod-
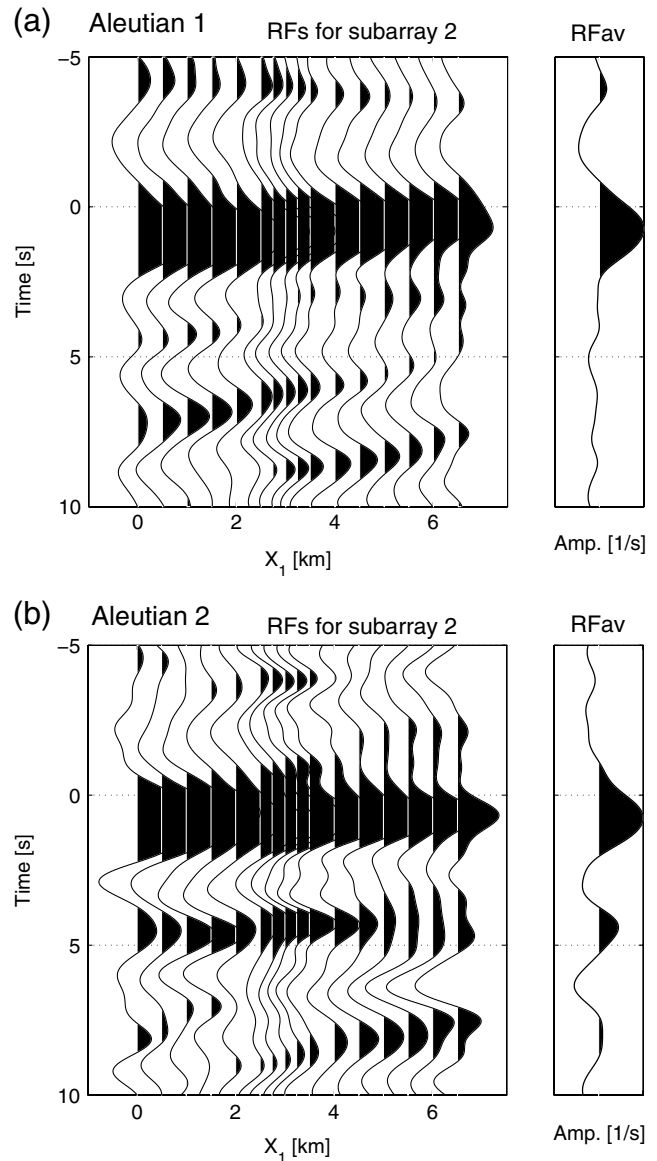

Figure 10. RFs for (a) event Aleutian 1, and (b) event Aleutian 2 (see Fig. 3). (left) All RFs for subarray 2 (see Fig. 2); (right) plot of the average over all RFs.

eling. However, after deconvolving *R* with the *Z* component, thus on the RF, both interfaces show a clear imprint. In Figure 11b we choose a central frequency close to the observed one of the Aleutian *P*-phase arrivals ($f_0 = 0.2$ Hz). Now the *Z*- and *R*-component responses and also the RF only show the event due to the Moho conversion clearly. *Pps* and *Ppp* interfere constructively to a phase with $t = 0.5$ s in the RF. In principle, this time shift with respect to $t = 0$ could be used to find the depth of the basement-basin interface.

For the field data RFs (Fig. 10), a similar time-shifted phase near $t = 0$ can be seen as in the forward modeled RF (Fig. 11b). For the field data, the time shift of the peak is 0.74 and 0.77 s for Aleutian 1 and 2, respectively. These time shifts are considerably larger than the time shift of the forward modeled RF (0.5 s). Yet, it is complicated to use this
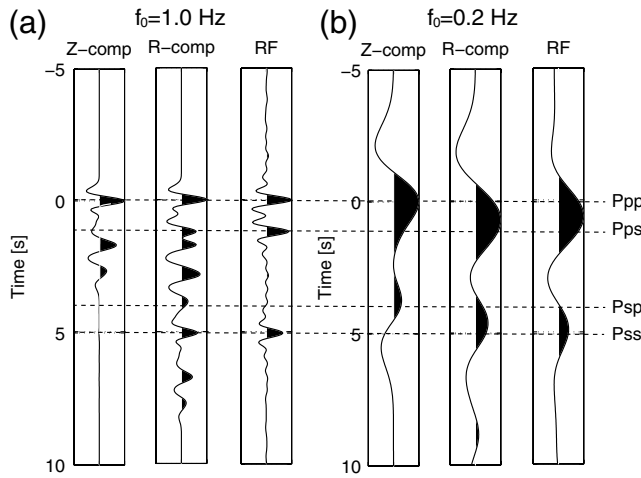
Figure 11. Synthetic *P*-wave forward scattered responses for the model in Figure 5a and a ray parameter of 0.04 s/km, for a source–time function composed of Ricker wavelets with a central frequency of (a) 1.0 Hz and (b) 0.2 Hz. To achieve the same sign of the phases as in Langston (1979) the *R*-component points away from the source and the *Z*-component points upward.

time shift to update the model. This time shift is caused by an interference and is not only dependent on the travel-time difference between *Ppp* and *Pps*, but also on the near-surface amplification of *Pps* with respect to *Ppp*. Furthermore, in addition to the basin–basement interface, there might be shallower interfaces that lead to conversions that also add to the interference pattern.

The other main phase in the forward modeled RF is due to the Moho conversion (*Pss*). This event seems to be well resolved in the average RF for Aleutian 2 (Fig. 10b). In the average RF for Aleutian 1 (Fig. 10a) the same event is not visible, possibly due to destructive interference with microseism related noise.

To map an observed travel-time difference to depth, a *P*- and *S*-wave velocity model would be required. Here we could use the one updated by body-wave SI. Otherwise, for example, a velocity model obtained by surface-wave inversion or body-wave tomography could be used.

Discussion and Conclusions

We analyzed 40 hours of data recorded over the Abu Gharadig basin in Egypt. In an earlier study we found the frequency band of 0.09–1.0 Hz to be dominated by body waves. To this band, we applied a variety of passive seismic methods with the goal to obtain the depth (variation) of the sedimentary basin. From the literature it is known that this interface is located at about 5-km depth. With body-wave SI we could extract *PP* and *SS* reflections from this interface. The *Z*-component responses contained a broad illumination band inline with a subarray, unlike the horizontal components. Consequently, the best-quality reflection responses were obtained for the vertical component. Using those, we could confirm the depth of the basin to be around 4.8 km.

Also, we could extract spatial travel-time differences of *PP* reflections, but we could not uniquely relate these to basin-depth topography or spatial variations within the basin. As a second technique we estimated the resonance spectrum of the basin, using the H/V. Using surface-wave noise, we found an extremum in the H/V (ellipticity) that is related to the complete sedimentary package. Using this extremum, we found a basin depth of 5.4 km. Using *S*-phase arrivals, we found two extrema in the H/V, which are probably related to the *S*-wave resonances of two distinct layers in the basin. Adding up their estimated thicknesses, we found a basin depth of 5.1 km. Third, with an RF study we could confirm the presence of a large interface in the upper crust. However, for the frequency range that was needed to achieve good quality RFs, the conversion on the basin–basement interface could not be observed directly. Instead, an interference pattern was seen between the *P* and *S* transmission. This interference pattern could not be inverted reliably for the basin depth.

Using a 40-hour passive record, we did succeed in finding the average depth of the basin, using body-wave SI. Also we found that the lateral variations of the basin floor are less than 100 m below the array. Thus, we could establish that the entire array is located within the same basin block.

For H/V a large number of approximations had to be made (equations 1–5). Moreover, the results could only be interpreted with some prior information about the basin, such as the amount of resonating layers expected. Therefore, H/V seems to be more suitable for testing a certain model rather than for exploration purposes.

Body-wave SI gave good results on the *Z* component, due to a balanced noise illumination inline with one of the subarrays. The retrieved responses on the horizontal components were of a lesser quality, due to missing illumination with steep angles of incidence and subdominant illumination not inline with the subarray.

Worldwide, basin depths may vary from virtually ground level to about 15 km (Laske and Masters, 1997). Body-wave H/V will be especially useful in delineating a basin when its depth does not exceed more than 3 km. For reliably delineating larger depths, body-wave noise would be required in the SF band. Ambient noise in the SF band is predominantly caused by the interaction of ocean swell waves with continental shelves (Webb, 2002). This interaction does not seem to induce body waves of any markable size. Hence, for larger depths, surface-wave H/V ratio would need to be used.

Body-wave SI, on the other hand, is easier to apply when the basin depth exceeds 2 km. For shallower interfaces, body-wave noise above 1 Hz would be required, which tends to be obscured by surface-wave arrivals. When noise below 1 Hz is used, reflections from shallower interfaces are covered by a spurious direct wave.

The third considered method, using teleseismic receiver functions, only becomes practical when the basin depth exceeds 5 km. In this case, the direct wave and converted wave could show up as individual events in the receivers function,

and their travel-time difference could easily be picked. In our study, we only had high-quality seismicity from distances exceeding 90°. This resulted in receiver functions with a rather low central frequency, which would only allow a basin-depth estimation if the depth were below 8 km. In principle, regional seismicity could be used to obtain receiver functions with a larger central frequency. However, crustal multipathing would make it tedious to interpret the results. Similar to an exploration-scale application (Van Manen *et al.*, 2003) a large number of receiver functions would need to be stacked before obtaining an interpretable signal from the basin–basement interface. In general it is unlikely that this large distribution of regional seismicity would be present, given a limited acquisition time.

A similar passive survey as discussed in this study could be upscaled by a factor of 20 to find a basin-depth map over a large region. In this case the inline station sampling would be about 10 km. For a total survey area of 100×100 km it may be assumed that the low-frequency seismicity is fairly constant. Still, a denser subarray would be required for beamforming the noise and to pick out the time windows with a favorable illumination. The large separation of the stations in the main array would only allow the retrieval of reflections for coinciding source and receiver position from the (relatively shallow) basin–basement interface. Therefore, a velocity model for the basin would need to be available through other means.

Data and Resources

Seismic data used in this study were provided by Shell Egypt NV and are proprietary. They cannot be released to the public. Events in the data were recognized by raytracing phase-arrival times from major earthquakes in the IRIS earthquake browser (www.iris.edu/ieb/) (last accessed August 2011). The raytracing was done with TTBOX, which is available at http://www.dr-knapmeyer.de/downloads/ (last accessed August 2011). All the maps were made with M_Map, which is available at http://www.eos.ubc.ca/~rich/map.html (last accessed August 2011).

Acknowledgments

References

Ammon, C. J. (1991). The isolation of receiver effects from teleseismic *P* waveforms, *Bull. Seismol. Soc. Am.* **81,** 2504–2510.

Asten, M. W., and J. D. Henstridge (1984). Array estimators and the use of microseisms for reconnaissance of sedimentary basins, *Geophysics* **49,** 1828–1837.

Bachu, S. (2003). Screening and ranking of sedimentary basins for sequestration of CO_2 in geological media in response to climate change, *Environ. Geol.* **44,** 277–289.

Barbosa, V. C. F., J. B. C. Silva, and W. E. Medeiros (1997). Gravity inversion of basement relief using approximate equality constraints on depths, *Geophysics* **62,** 1745–1757.

Bosworth, W., A. El-Hawat, D. Helgeson, and K. Burke (2008). Cyrenaican "shock absorber" and associated inversion strain shadow in the collision zone of northeast Africa, *Geology* **36,** 695–698.

Field, E. H., and K. H. Jacob (1995). A comparison and test of various site-response estimation techniques, including three that are not reference-site dependent, *Bull. Seismol. Soc. Am.* **85,** 1127–1143.

Franssen, R., and E. H. Hoogerduijn-Strating (2006). Discovering and developing a deep Jurassic play in the mature Western Desert-Abu Gharadig Basin, Egypt, *SPE Europec/EAGE Annual Conference and Exhibition*, Vienna, Austria, 12–15 June 2006, SPE 100125.

Galetti, E., and A. Curtis (2011). Generalized receiver functions and seismic interferometry, *Tectonophysics* **532–535,** 1–26.

Herak, M. (2008). ModelHVSR-A MATLAB® tool to model horizontal-to-vertical spectral ratio of ambient noise, *Comput. Geosci.* **34,** 1514–1526.

Hoogerduijn-Strating, E. H., and W. Postuma (2008). Reservoir compartimentalization in the JG field Western Desert Egypt, *SPE Europec/EAGE Annual Conference and Exhibition*, Rome, Italy, 9–12 June 2008, SPE 113865.

Isacks, B. L., and C. Stephens (1975). Conversion of *Sn* to *Lg* at a continental margin, *Bull. Seismol. Soc. Am.* **65,** 235–244.

Lacoss, R. T., E. J. Kelly, and M. N. Toksöz (1969). Estimation of seismic noise structure using arrays, *Geophysics* **34,** 21–38.

Langston, C. A. (1979). Structure under Mount Rainier, Washington, inferred from teleseismic body waves, *J. Geophys. Res.* **84,** 4749–4762.

Laske, G., and G. Masters (1997). A global digital map of sediment thickness, *Eos Trans. AGU* **78,** F483.

Lermo, J., and F. J. Chávez-García (1994). Are microtremors useful in site response evaluation? *Bull. Seismol. Soc. Am.* **84,** 1350–1364.

Martini, F., I. Lokmer, K. Jonsdottir, C. J. Bean, F. Hauser, M. Möllhoff, L. de Barros, J. T. Doherty, C. Ryan, and J. Mongan (2011). A passive low frequency seismic experiment in the Albertine Graben, Uganda: Basin structure control? (Extended abstract PAS19), *EAGE 3rd Passive Seismic Workshop-Actively Passive*, Athens, Greece, 29 March 2011.

Nakamura, Y. (2000). Clear identification of fundamental idea of Nakamura's technique and its applications, *Proc. of the 12th World Conf. on Earthquake Engineering*, Auckland, New Zealand, Paper No. 2656.

Ruigrok, E. N., X. Campman, D. Draganov, and K. Wapenaar (2010). High-resolution lithospheric imaging with seismic interferometry, *Geophys. J. Int.* **183,** 339–357.

Ruigrok, E. N., X. Campman, and K. Wapenaar (2011). Extraction of *P*-wave reflections from microseisms, *Compt. Rendus Geosci.* **343,** 512–525.

Salem, A., S. Williams, D. Fairhead, R. Smith, and D. Ravat (2008). Interpretation of magnetic data using tilt-angle derivatives, *Geophysics* **73,** no. 1, L1–L10.

Schuster, G. T. (2009). *Seismic Interferometry* Cambridge University Press, Cambridge, UK.

Seber, D., M. Vallve, E. Sandvol, and D. Steer (1997). Middle East tectonics: Application of geographic information systems, *GSA Today* **7,** 1–5.

Shapiro, N. M., M. Campillo, L. Stehly, and M. H. Ritzwoller (2005). High-resolution surface-wave tomography from ambient seismic noise, *Science* **307,** 1615–1618.

St. John, B., A. W. Bally, and H. D. Klemme (1984). *Sedimentary provinces of the world—Hydrocarbon productive and non-productive*, AAPG Special Publications, Tulsa, Oklahoma.

Storchak, D. A., J. Schweitzer, and P. Bormann (2003). The IASPEI standard seismic phase list, *Seismol. Res. Lett.* **74,** 761–772.

Toksöz, M. Nafi (1964). Microseisms and an attempted application to exploration, *Geophysics* **29,** 154–177.

Tsai, N. C. (1970). A note on the steady-state response of an elastic half-space, *Bull. Seismol. Soc. Am.* **60,** 795–808.

Van Manen, D., J. O. A. Robertsson, A. Curtis, R. Ferber, and H. Paulssen (2003). Shear wave statics using receiver functions, *Geophys. J. Int.* **153,** F1–F5.

Wapenaar, K., and J. T. Fokkema (2006). Green's functions representations for seismic interferometry, *Geophysics* **71,** no. 4, SI33–SI46.

Wapenaar, K., D. Draganov, R. Snieder, X. Campman, and A. Verdel (2010). Tutorial on seismic interferometry: Part 1-Basic principles and applications, *Geophysics* **75,** no. 5, 75A195–75A209.

Webb, S. C. (2002). Seismic noise on land and on the sea floor, *Int. Geophys.* **81,** 305–318.

Xia, J., R. D. Miller, and C. B. Park (1999). Estimation of near-surface shear-wave velocity by inversion of Rayleigh waves, *Geophysics* **64,** 691–700.

Yilmaz, O., and S. M. Doherty (2000). *Seismic data analysis: Processing, inversion, and interpretation of seismic data* SEG Abstracts, Tulsa, Oklahoma, 12 pp.

Delft University of Technology
Department of Geoscience and Engineering
Stevinweg 1, 2628 EC Delft
The Netherlands
    (E.R., K.W.)

Shell Global Solutions International B.V.
Kessler Park 1, 2288 GS Rijswijk
The Netherlands
    (X.C.)